ELSEVIER

Chemical Engineering Journal 142 (2008) 95–108

Chemical Engineering Journal

www.elsevier.com/locate/cej

Modelling mass transfer in an aerated 0.2 m^3 vessel agitated by Rushton, Phasejet and Combijet impellers

Pasi Moilanen *, Marko Laakkonen, Olli Visuri, Ville Alopaeus, Juhani Aittamaa

Helsinki University of Technology, Laboratory of Chemical Engineering, P.O. Box 6100, FIN-02015 HUT, Finland

Received 19 September 2007; received in revised form 7 January 2008; accepted 21 January 2008

Abstract

We assembled a set of models that allows investigation of local variables that are difficult to measure, validation of mechanistic physical models, and comparison of different numerical solutions. Population balances (PB) for bubbles were combined with local flow modelling in order to investigate G–L mass transfer in an air–water system. Performance of three different impeller geometries was investigated: Rushton (RT), Phasejet (PJ) and Combijet (CJ). Simulations were compared against experimental mixing intensity, gas hold-up, vessel-averaged volumetric mass transfer rates (k_La), and local bubble size distributions (BSDs).

The simulations qualitatively predict k_La's with different impellers at the fully dispersed flow region and gave new insight on how k_La is formed and distributed in the stirred vessels. The used bubble breakage and coalescence models are able to describe both air–water and viscous non-Newtonian G–L mass transfer. Difference between experimental mass transfer rates of the three impellers was within experimental error, even trough the flow patterns, gas distribution, and local BSDs differ considerably. The population balance for bubbles was modelled in two different ways, with multiple size groups (MUSIGs) and with the bubble number density (BND) approach. MUSIG calculations took over twice as much computational time than BND, but there was little difference in the results. The Rushton turbine k_La was described with best accuracy, which is not surprising since most phenomenological models are fitted based on RT experiments. We suggest that these models should be validated over a wider range of vessel geometries and operating conditions.

Keywords: Mass transfer; Stirred tank; Hydrodynamics; Mixing; Population balances

1. Introduction

Stirred reactors are among the most widely used reactors in chemical industries. They offer unmatched flexibility and control over transport processes occurring in the reactor [1]. Gas–liquid mass transfer is often the limiting reaction step when dealing with only slightly soluble gasses like oxygen [2]. In order to make successful designs the behaviour of the reactor needs to be understood in detail. Often the acquirement of local experimental information from reactors is difficult or too costly. An alternative for investigating gas–liquid hydrodynamics, mass transfer, vessel geometries, operating conditions and scale-up effects is to develop rigorous models incorporating all relevant phenomena. Dimensionless correlations are widely used in reactor design, but they are only reliable if the operating parameters and the vessel geometry are similar. The effects of vessel geometry and operating parameters are hard to predict accurately. Computational fluid dynamics (CFD) is a tool that can be used to investigate a reactor in great detail. Phenomenological models can be used to accurately simulate large industrial reactors even with high scale-up ratios [3].

Population balances (PB) like multiple size group (MUSIG) and bubble number density (BND) have been recently used to describe G–L stirred vessels. Our work has been done with MUSIG and a Rushton turbine (RT) [4,5], while others have used BND to describe double RT's [6,7], and compared a RT with the lightnin A315 impeller [8]. With bubble columns there exists a single comparison of BND versus MUSIG simulation [9], but the operating conditions are not comparable with stirred

Abbreviations: BND, bubble number density; BSD, bubble size distribution; CFD, computational fluid dynamics; CJ, Ekato Combijet; CSP, capillary suction probe; DO, dissolved oxygen; MFOR, multiple frames of reference; MUSIG, multiple size group; PJ, Ekato Phasejet; RSM, Reynolds stress model; RT, Rushton turbine; SST, shear stress transport; vvm, volume of gas feed per liquid volume in minute (m^3(gas)/(m^3(liquid) min)); PB, population balance.

* Corresponding author. Tel.: +358 9 451 2638; fax: +358 9 451 2694.
E-mail address: pasi.moilanen@hut.fi (P. Moilanen).

1385-8947/$ – see front matter © 2008 Elsevier B.V. All rights reserved.
doi:10.1016/j.cej.2008.01.033

Nomenclature

a	interfacial area (m^2/m^3(liquid))
c	concentration (wt.% or mg/L)
c^*	equilibrium concentration (mg/L)
C_1	constant (0.3)
C_D	bubble drag coefficient
d	characteristic bubble group size (m)
d_{32}	Sauter mean diameter = $\Sigma d^3/\Sigma d^2$ (m)
D	diameter (m)
D_L	liquid phase diffusion coefficient (m^2/s)
$E(d)$	bubble aspect ratio
g	acceleration due to gravitation (9.81 m/s^2)
G	geometric ratio
$h\langle d_k,d_p\rangle$	coalescence frequency (m^3/s)
H	height of liquid level (m)
i, j	index number of a bubble class
k_L	mass transfer coefficient in liquid film (m/s)
k_La	volumetric mass transfer coefficient (s^{-1})
Mo	Morton number (Eq. (5))
n	bubble number density (m^{-3})
$n(d)$	number density (Eq. (8))
N	number of bubbles
R	radius of the spindle (m)
Re	bubble Reynolds number (Eq. (3))
T	tank diameter (m)
U_{slip}	bubble slip velocity (m/s)
v	velocity (m/s)
$v(d)$	volume density (Eq. (9))
W	baffle width (m)
We	Weber number (Eq. (15))
S	source/sink term ($m^{-3}\,s^{-1}$)

Greek letters

α	volume fraction of gas
γ	shear rate (s^{-1})
ε	turbulent energy dissipation (W/kg(liquid))
η	coalescence efficiency
θ	temperature (°C)
μ	viscosity (Pa s)
ρ	density (kg/m^3)
σ	surface tension (N/m)

Subscripts

20	at 20 °C
app	apparent
baf	baffle
BR	breakage
bub	bubble
C	continuous
CO	coalescence
CR	critical
imp	impeller
liq	liquid
max	maximum
min	minimum
spa	sparger
tot	total

tanks. In this work effect of three impeller geometries on G–L mass transfer was investigated with two different PB approaches, no similar work on stirred vessels was found in the literature. In this work we take a closer look at the effect of impeller geometry on the G–L mass transfer in stirred tanks.

2. Experimental

2.1. Experimental system and vessel geometry

Gas–liquid mass transfer and hydrodynamics were measured for air–water dispersion. The experiments were made in a 0.2 m^3 stirred tank. The dimensions of the fully baffled vessel are: $T = 0.64$ m, $H = T$, $C_{imp} = T/3$, $W = T/10$ and $C_{baf} = T/20$. Surface baffling was used to avoid surface aeration. The gas was introduced through a ring sparger $D_{spa} = T/4$ below the impeller. Three impellers were used in the experiments: a 6-blade radial Rushton turbine $D_{imp} = T/3$, a radial 6-blade Ekato Phasejet (PJ) $D_{imp} = 0.44T$ and a 3-blade mixed flow Ekato Combijet (CJ) $D_{imp} = 0.46T$. Impeller geometries and computational surface grids are presented in Fig. 1.

The measured quantities include vessel-averaged gas hold-up, mixing intensity, bubble size, and mass transfer. The vessel-averaged hold-up was measured from the change in the liquid level surface. The mixing intensity was measured from the angular momentum of the impeller. The mass transfer was measured with a dynamic technique using a polarographic oxygen probe (LT Lutron, DO-5510). Surface tension was measured with KSV Sigma 70 tensiometer and viscosity was measured with Brookfield DV-E viscometer. The experimental value of $\sigma = 70$ mN/m was used in the simulations. The volumetric mass transfer coefficient is calculated from the dissolved oxygen (DO) measurements, a natural logarithm of $c^*_{DO} - c_{DO}$ was taken and plotted against time. Then the angular coefficient (k_La) of the curve was calculated, the result was normalized to 20 °C [10].

$$k_La_{20} = \frac{k_La}{1.022^{\theta-20}} \quad (1)$$

2.2. Capillary suction probe

The capillary suction probe (CSP) of Barigou and Greaves [11,12] can be used for opaque dispersions and large holdups giving an edge over optical methods. The detectable bubble range is roughly 1–5 times the inner capillary diameter, which was 1.2 mm in our experiments. The minimum bubble size is determined by the inner diameter of the capillary, smaller bubbles are not detected. Large bubbles in turn generate long slugs that may break or distort in the capillary. A calibration is needed due to a liquid film at the capillary inner walls and slug expansion

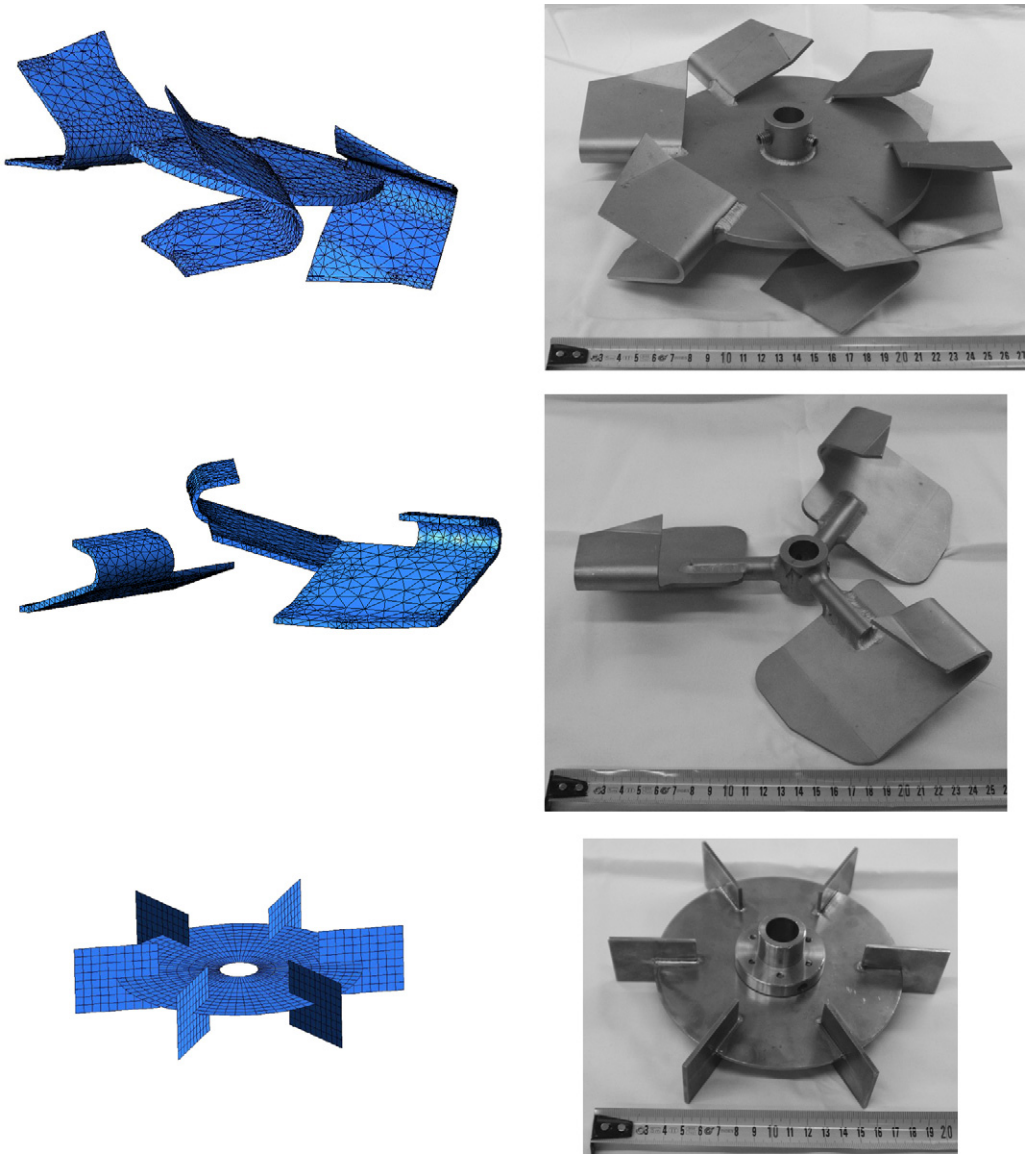

Fig. 1. Surface grids and impeller photographs (scale in cm).

by the pressure drop in the capillary. The viscosity of the liquid must be low due to pressure drop and the capillary length is limited. The liquid must be free of particulate impurities that cause measurement errors and plugging of capillary. An appropriate suction speed is needed to ensure that various sized bubbles are sucked into the capillary with equal probability, i.e. 'isokinetically' in order to measure bubble size distribution (BSD) reliably. The CSP has been recently used [13,14] in stirred vessels.

3. CFD modelling

The CFD modelling was done with CFX 5.7.1. Impeller motion was mainly modelled with the steady-state multiple frames of reference technique (MFOR). A few transient simulations were made with a sliding grid. The outer computational domain was always modelled with a structured hexahedral mesh. The baffling and Rushton impeller were modelled as thin surfaces, whereas the CJ and PJ have a finite thickness. The RT mesh is hexahedral, whereas the complex PJ and CJ geometries required an unstructured tetrahedral mesh. For RT and PJ a 180° segment of the vessel was modelled with periodic boundaries, the CJ impeller required the modelling of the full 360° geometry. The number of computational nodes was >120,000 in every case, the effect of grid resolution was addressed in our previous work [5,15]. The liquid surface is assumed flat with a degassing condition, the volume of dispersion is considered to be constant. The turbulence was described by the SST model. The SST combines the best parts of both the k–ε and the k–Ω turbulence models [16]. The turbulent energy dissipation is scaled in the bubble coalescence and breakage models according to experimental power consumption by assuming that all mechanical energy dissipates through turbulence. From the possible G–L closure models [17,18] only bubble drag was used, since it is the dominant interfacial force in gas–liquid flow.

3.1. Bubble drag

The use of customised models for air–water dispersions was intentionally avoided, in order to gain a wider range of applicability; these models have previously been used to model viscous gas–liquid flow agitated by RT [5]. A bubble drag model of Tzounakos et al. [19] is used. It has been originally developed for slightly viscous power-law fluids.

$$C_D = \begin{cases} \frac{24}{Re}(1 + 0.173Re^{0.657}), & Re < 135 \\ 0.95, & Re > 135 \end{cases}, \quad (2)$$

where

$$Re = \frac{d_{32}U_{slip}\rho_c}{\mu_{bub}} \quad (3)$$

To account for the effect of non-spherical bubbles on the drag-correlation a bubble shape correlation [20] is used.

$$E(d) = \begin{cases} 1.1, & Re\,Mo^{0.078} < 4 \\ 1.88(Re\,Mo^{0.078})^{-0.386}, & 4 \le Re\,Mo^{0.078} \le 15 \\ 0.66, & 15 < Re\,Mo^{0.078} \end{cases}, \quad (4)$$

where

$$Mo = \frac{g\mu_{app}^4}{\rho_C\sigma^3} \quad (5)$$

The total shear experienced by a group of bubbles is formed from two terms: the liquid flow induced and the bubble-generated shear. This shear rate is used in the calculation of liquid viscosity for the bubble slip velocity. The bubble drag model is developed so that it can be used for non-Newtonian fluids as well.

$$\gamma_{tot} = \gamma_{liq} + \frac{U_{slip}}{d_{32}}E(d) \quad (6)$$

3.2. Multiple size group model

The MUSIG model [21] has been developed for handling polydispersed multiphase flows. This population balance model allows the prediction of the local BSD based on physical phenomena, allowing the interfacial area to be calculated more accurately. In the MUSIG model it is assumed that bubbles of varying size have the same slip velocity, which is calculated based on local Sauter mean diameter (d_{32}). This means that flow cannot segregate the bubbles based on their size, which is a notable limitation.

Bubble breakage and coalescence models are needed as closures in population balances. The bubble breakage rate model of Luo and Svendsen [22] is used in integrated form with the daughter bubble size distribution of Lehr et al. [23]. Bubble coalescence is calculated from Coulaloglou and Tavlarides [24] with the coalescence efficiency model from Chesters [25]. The population balance model was presented in our previous work [5]. The bubble breakage and coalescence parameters have been fitted inversely with a computationally less demanding multiblock model and reported in our previous work [26]. The parameter fitting was done based on experiments from the same 0.2 m^3 Rushton agitated vessel with aqueous xanthan solutions of 0–0.75 wt.%. In our previous work it was shown that the xanthan fitted model performs reasonably with air–water systems [5]. A geometric discretisation of bubbles is used.

$$d(i) = d_{min}G^i, \qquad \Delta d = \frac{(d_{min}G^{i+1}) - (d_{min}G^{i-1})}{2}, \quad (7)$$

which produces a dense discretisation for small bubbles and a loose for larger ones. Ten size categories used the simulations as a compromise between solution accuracy and computational burden. With values of $G = 1.45$ and $d_{min} = 0.33$ mm the discretisation covers a BSD range of 0.33–16.53 mm. The number density is defined as

$$n(d_i) = \frac{d_{max} - d_{min}}{\Delta d_i}\frac{N_i}{\sum_{j=1}^{NC} N_j} \quad (8)$$

The volume density is defined as

$$v(d_i) = \frac{d_{max} - d_{min}}{\Delta d_i}\frac{N_i d_i^3}{\sum_{j=1}^{NC} N_j d_j^3} \quad (9)$$

3.3. The bubble number density model

By modelling bubble number density the variation of local bubble size can be simulated with just one scalar, which decreases the computational burden when compared against PBs with multiple classes. The BND is calculated from the gas volume, which in turn is calculated from the gas mass balance. This method developed by Wu et al. [27] has been recently used by Kerdouss et al. [6] and Lane et al. [8] to simulate gas–liquid flow in stirred vessels. The CFD simulation is Eulerian, the BND attached to the dispersed air-phase having convection and diffusion. The changes in BND are caused by bubble coalescence and breakage. The used model is based on the recent work of Lane et al. [8] and it is presented in the following equations:

$$\frac{\partial n}{\partial t} = S_{BR}n - S_{CO}n^2 \quad (10)$$

$$n = \frac{\alpha}{(\pi/6)d^3} \quad (11)$$

$$S_{BR} = C_{BR}(1-\alpha)\left(\frac{\varepsilon}{d^2}\right)^{1/3}\exp\left(\frac{We_{CR}}{We}\right), \quad We > We_{CR} \quad (12)$$

$$S_{BR} = 0, \quad We < We_{CR} \quad (13)$$

$$S_{CO} = C_{CO}(1-\alpha)\eta_{CO}\varepsilon^{1/3}d^{7/3} \quad (14)$$

where

$$We = \frac{\rho_C d^{5/3}\varepsilon^{2/3}}{\sigma} \quad (15)$$

$$\eta_{CO} = \exp\left(-\sqrt{\frac{We}{8}}\right) \quad (16)$$

The used parameter values were $We_{CR} = 1.5$, $C_{CO} = 0.05$, and $C_{BR} = 0.075$. The bubble number balance is modified by source/sink terms in the computational domain, the inlet boundary condition is set at $n = 1.5 \times 10^5$ to represent a bubble size of >10 mm. The results cannot directly be compared with multiple bubble class simulations, since the used breakage and coalescence models are not identical.

3.4. Mass transfer model

The mass transfer coefficient in the liquid film (k_L) is calculated from Ref. [28]. The value of C_1 was set at 0.3, based on multiblock model simulations [26]. The local interfacial area (a) is calculated from the population balance model. The diffusivity of oxygen (D_L) in water is 1.98×10^{-9} m^2/s at 20 °C.

$$k_L = C_1 \sqrt{D_L} \left(\frac{\varepsilon \rho_C}{\mu_C} \right)^{1/4} \quad (17)$$

When dealing with poorly soluble gasses, no chemical reaction and small differences in the diffusivities of the components, it is reasonable to use a simple approach for mass transfer modelling. The local volumetric mass transfer coefficient ($k_L a$) is calculated from local gas–liquid area and local k_L, without taking into account the actual driving force of concentration difference from equilibrium. This vessel-averaged $k_L a$ can be used in simpler reactor models, which require far less computational effort. When mass transfer is very fast, the heterogeneous nature of agitated dispersion begins to affect the calculation of $k_L a$ [15,29].

4. Results and discussion

The PB simulations with 10 bubble classes were made at mixing intensities of 0.66 and 2.1 W/kg (liquid) and a constant gassing rate of 0.7 vvm. The vessel-averaged measurements include vessel-averaged gas hold-up, mass transfer rate and mixing intensity. The CSP provides local BSDs in several measurement locations, which can be used to compare the local BSDs predicted by CFD against measured BSDs.

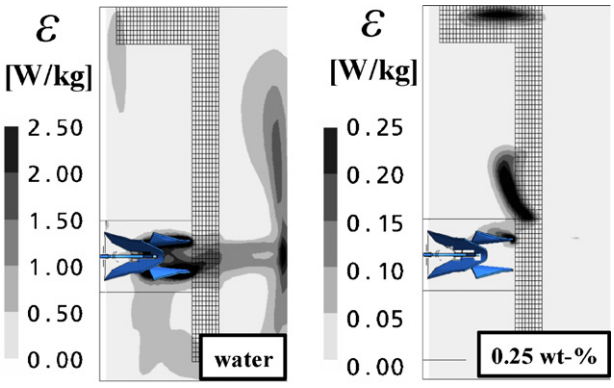

Fig. 2. Turbulent energy dissipation. Experimental power consumption 2.1 W/kg(liquid), k–Ω turbulence model, one-phase water and 0.25 wt.% xanthan solution. Note the different scales.

4.1. Turbulence modelling in the transitional regime

We tried to model G–L mass transfer in viscous fluids in similar conditions as in our previous work [5], but the simulations failed with Ekato impellers. The simulations converged with viscous fluids (0.25–2.5 wt.% aqueous xanthan gum) but the turbulent energy dissipation seems unrealistic; the highest values of turbulence are not in the impeller discharge stream (Fig. 2). For PJ at 0.25 wt.% xanthan, the simulated vessel-averaged turbulent energy dissipation is 0.008 W/kg while the measured is 2.1 W/kg. In water simulations turbulent energy dissipation is underpredicted (Table 1), but its distribution is reasonable (Fig. 2). All tested two equation turbulence models (k–ε, k–Ω, SST) produced similar results whereas the RSM model diverged; the rate of gassing, different computational grid designs, different initialisations and solver under relaxation was tried without success. The problems with turbulence modelling are probably connected to the local flow conditions, mainly affected by the impeller type, rotation speed, gassing rate and fluid viscosity model. There is a need for turbulence models that behave reasonably in the transitional turbulence regime. The lower apparent viscosity due to higher shear in the impeller discharge flow may

Table 1
Global results from experiments (normal) compared against MUSIG (parenthesis), BND (italic) and MUSIG with sliding grid (underlined) simulations

Experimental													
Impeller	RT	RT	RT	RT	PJ	PJ	PJ	PJ	CJ	CJ	CJ	CJ	CJ
Gas hold-up (vol-%)	4.83	4.83	6.46	6.46	5.50	5.50	8.75	8.75	4.80	4.80	7.34	7.34	7.34
Turbulent energy dissipation (W/kg)	0.66	0.66	2.1	2.1	0.66	0.66	2.1	2.1	0.66	0.66	2.1	2.1	2.1
Volumetric mass transfer rate (s^{-1})	0.039	0.039	0.054	0.054	0.036	0.036	0.055	0.055	0.037	0.037	0.058	0.058	0.058
Simulated	MUSIG	BND	MUSIG	BND	MUSIG	BND	MUSIG	BND	MUSIG	BND	MUSIG	MUSIG	BND
Gas hold-up (vol-%)	(2.83)	*2.90*	(4.98)	*4.97*	(4.83)	*4.43*	(11.13)	*8.83*	(4.99)	*4.56*	(8.61)	8.60	*7.94*
Turbulent energy dissipation (W/kg)	(0.55)	*0.32*	(1.67)	*1.02*	(0.23)	*0.24*	(0.80)	*0.76*	(0.24)	*0.24*	(0.87)	0.80	*0.87*
Volumetric mass transfer rate (s^{-1})	(0.021)	*0.017*	(0.054)	*0.041*	(0.029)	*0.019*	(0.091)	*0.040*	(0.039)	*0.029*	(0.113)	0.109	*0.096*
Shear rate (s^{-1})	(8.47)	*9.84*	(12.06)	*14.13*	(15.87)	*16.07*	(25.49)	*25.12*	(12.35)	*12.37*	(19.03)	18.59	*18.98*
Eddy viscosity (Pa·s)	(1.71)	*1.02*	(2.42)	*1.52*	(0.83)	*0.86*	(1.19)	*1.20*	(0.98)	*0.99*	(1.48)	1.45	*1.49*
Average liquid velocity (m/s)	(0.35)	*0.36*	(0.51)	*0.54*	(0.51)	*0.52*	(0.85)	*0.84*	(0.44)	*0.44*	(0.69)	0.67	*0.69*
Bubble slip velocity (cm/s)	(20.06)	*19.39*	(19.24)	*20.03*	(20.84)	*22.42*	(18.80)	*23.85*	(20.5)	*20.8*	(19.1)	19.6	*20.0*
Bubble size (mm)	(3.08)	*2.89*	(2.78)	*3.04*	(3.31)	*3.88*	(2.75)	*4.23*	(3.13)	*3.24*	(2.54)	2.64	*2.84*
Interfacial area (m^2/m^3 (dispersion))	(57.4)	*48.4*	(111.8)	*88.4*	(74.9)	*51.8*	(190.1)	*87.2*	(93.3)	*71.0*	(199.1)	189.6	*168.0*

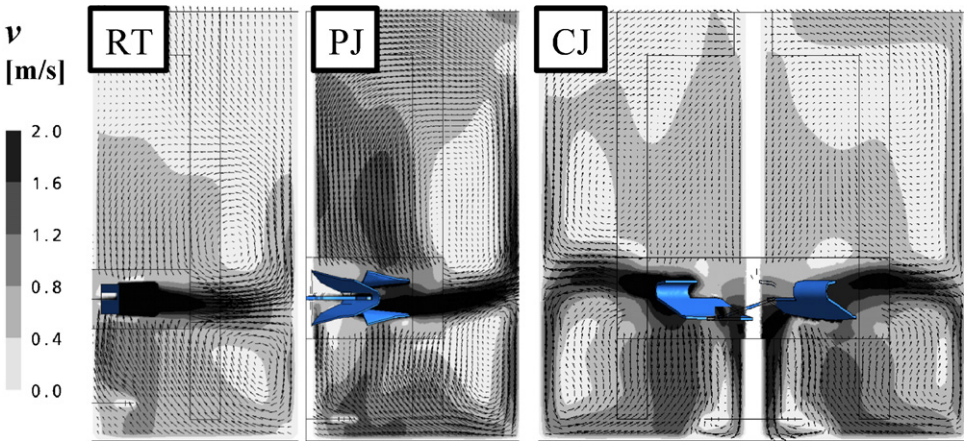

Fig. 3. Liquid velocity profiles and vectors for three different impellers (2.1 W/kg, 0.7 vvm).

explain why the turbulence model predictions with RT were successful. These simulations demonstrate that a change in the vessel geometry that alters local flow conditions may result in unexpected modelling difficulties at transient turbulence regime.

4.2. Flowfield comparison

The effects of impellers on the reactor performance have been recently studied [30–32]. The flowfields predicted by CFD for air–water system are illustrated in Figs. 3 and 4. The RT behaves as expected producing two re-circulating flows below and above the impeller plane. The PJ produces a similar flow pattern, with the exception that the upper re-circulating loop is larger. There seems to be more fluctuation in the flowfield, which may be caused by the increased interaction between the impeller and baffles, which is expected with large diameter impellers. The flowfield generated by the CJ is interesting, since the impeller looks like upwards pumping axial impeller at first glance. But the CJ forms a strong lower re-circulation loop, which keeps the gas hold-up high and creates a relatively weak and chaotic flow above the impeller plane. It is worth mentioning that the PJ and CJ impellers have a relatively stabile power-number with increasing gassing rate, resulting in easier scale-up and reactor design than with the RT.

CJ has the largest diameter and only three impeller blades create stronger interactions with the baffles. This brings about the question of modelling impeller motion. A more accurate

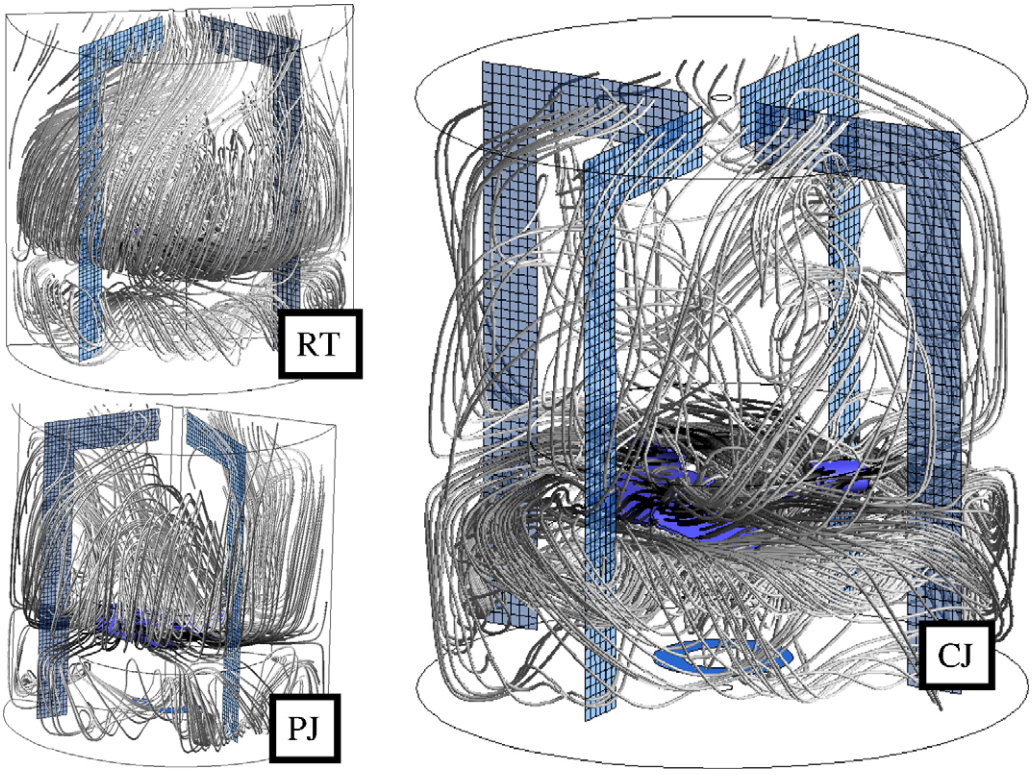

Fig. 4. Air flow field for all impellers (2.1 W/kg, 0.7 vvm); in dark areas the air velocity is high. Note the chaotic flowfield above the Combijet impeller.

description may require a transient sliding mesh approach in the impeller modelling. A sliding mesh simulation was made for the CJ; it slightly underpredicts the vessel-averaged k_La (3.7%) and a (4.8%) when compared to the corresponding MFOR simulation (Table 1). With RT and PJ the effect on k_La was below 1%, so the results are not presented. The vessel-averaged values appear to be almost the same, but there is local variation. We used a steady-state MFOR approach in impeller modelling in order to cut down the computational burden of simulations.

In the simulations gas is collected in the centres of strong re-circulating flows. However, local gas volumes larger than 50% seem unrealistic. This may be caused by the RANS approach in the turbulence modelling that neglects fluctuation of the liquid flow. In reality time-dependent turbulent eddies would disperse some of the gas from the centre of re-circulating flows. Another implausible thing is the downward flow below the CJ near the axis of vessel, while a strong upward flow from the lower re-circulating flow is right next to it. This generates a region of high turbulence right above the gas feed, generates small bubbles thus increasing the mass transfer area considerably (Figs. 3 and 5a–e).

4.3. CSP experiments

The measurement of local bubble sizes is challenging, most of the methods are not suitable for studying dense dispersions away from the vessel walls. In a previous study [13] the CSP was compared against other experimental methods and performed well

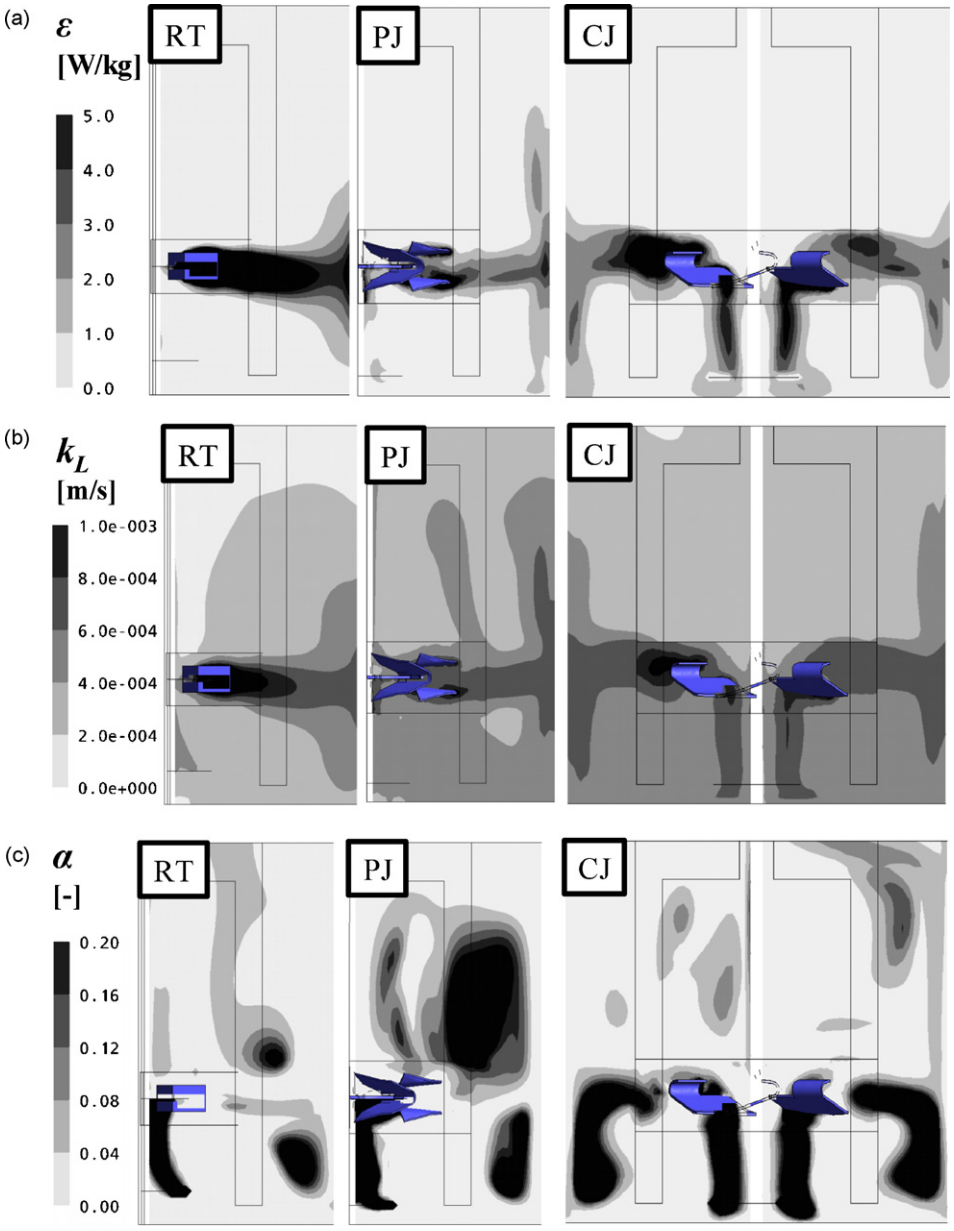

Fig. 5. (a) Local turbulent energy dissipation (2.1 W/kg, 0.7 vvm). (b) Local mass transfer coefficient in the liquid film (2.1 W/kg, 0.7 vvm). (c) Local gas hold-up (2.1 W/kg, 0.7 vvm). (d) Local Sauter mean diameter (2.1 W/kg, 0.7 vvm). (e) Local volumetric mass transfer coefficient (2.1 W/kg, 0.7 vvm).

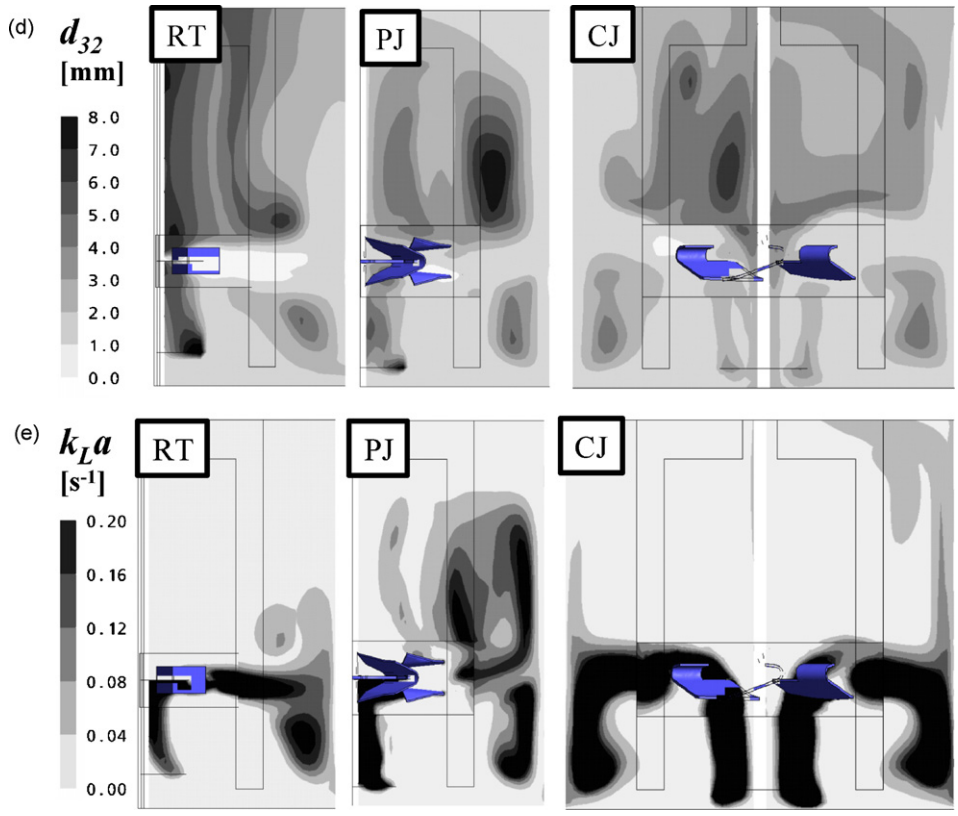

Fig. 5. (*Continued*).

with air–water dispersions. The experimental points are located in the mid-plane between baffles. The distances [mm] from vessel wall are A(32), B(104), C(168) and from the vessel bottom H(70), G(201), E(422) (Fig. 6a). The comparison of the simulated and experimental volumetric BSDs is not straightforward. The comparison between number density distributions is not reasonable, since the CSP is unable to detect them (Fig. 6b). The simulation always produces a peak of the number density distribution below the detection range of the CSP. If all simulated results (0–14 mm) are presented, the BSDs will look similar to Fig. 6c. A reasonable approach is to investigate the local BSD in the CSP measurement range (1.0–6.2 mm) by scaling results to fit $\sum_{i=1} v(d_i)\,\Delta d_i = 1$. This approach allows investigating the change in the shape of BSDs in greater resolution. The experimental local volumetric BSDs are compared against CFD simulations (Fig. 7a–d). Simulated pointwise Sauter mean diameters are compared against experiments in Table 2. With CJ spatial differences are considerable, so the simulated value was an average between all the four baffle mid-planes. With the RT and PJ there was only one intact baffle mid-plane due to the periodic boundary conditions.

First by looking at the volumetric CSP results it can be said that results for all impellers have similar trends. The bubble size is typically the smallest (BG) near the impeller tip and the largest (CE) in above the impeller near the centre of the vessel. From BG ⇒ AG and BH ⇒ AH the Sauter mean diameter increases, while it decreases from CE ⇒ BE ⇒ AE. The RT and PJ have very similar BSDs around the vessel, this can be expected since the overall flow patterns of the impellers are very similar (Figs. 3 and 4). The bubble size in the impeller discharge

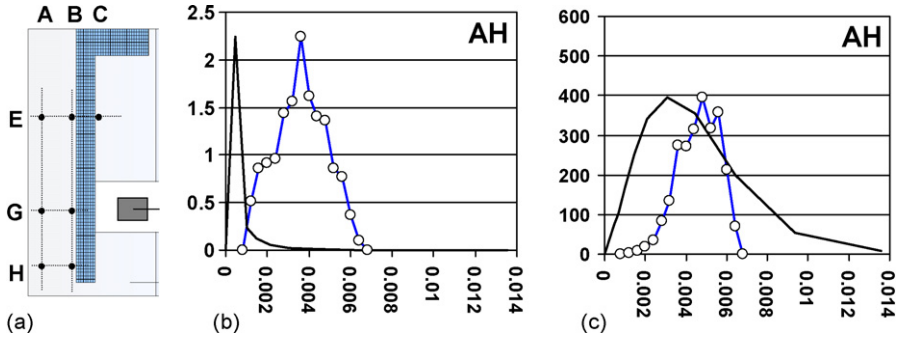

Fig. 6. (a) Schematic of sampling points in CSP experiments. (b) Bubble number density against bubble size (m), scaled according to corresponding peak height. (c) Bubble volume density against bubble size (m), scaled according to corresponding peak height (RT, 0.7 vvm, 2.1 W/kg, location AH).

flow (AG/BG) is smaller than with CJ. The measured bubble sizes can be explained reasonably: in the impeller discharge flow the turbulence/bubble breakage is the largest and the bubble size is the smallest. The largest bubble sizes can be found in areas where large bubbles are trapped in a downward flow (CE/AH) or alternatively in areas of high gas hold-up, where bubble coalescence is dominant. It seems that the measured BSDs are slightly distorted. The ends of the bubble size range are more likely to fail detection of a bubble, thus relatively raising the BSD in the middle range and the peak. The simulated BSD is almost every time 'flatter' than the measured one. The BSD simulations seem to slightly underpredict the d_{32} and the peak of the volume density distribution (Fig. 7a–d). It can be said that the used model can predict the BSD trends of the vessel quite accurately, even if there is some mismatch in actual values. It is notable that the point-averaged d_{32} does not necessarily correlate with the vessel-averaged value (Tables 1 and 2).

4.4. MUSIG simulations

It is highlighted here that the way the experimental and simulated $k_L a$ are calculated include several simplifications,

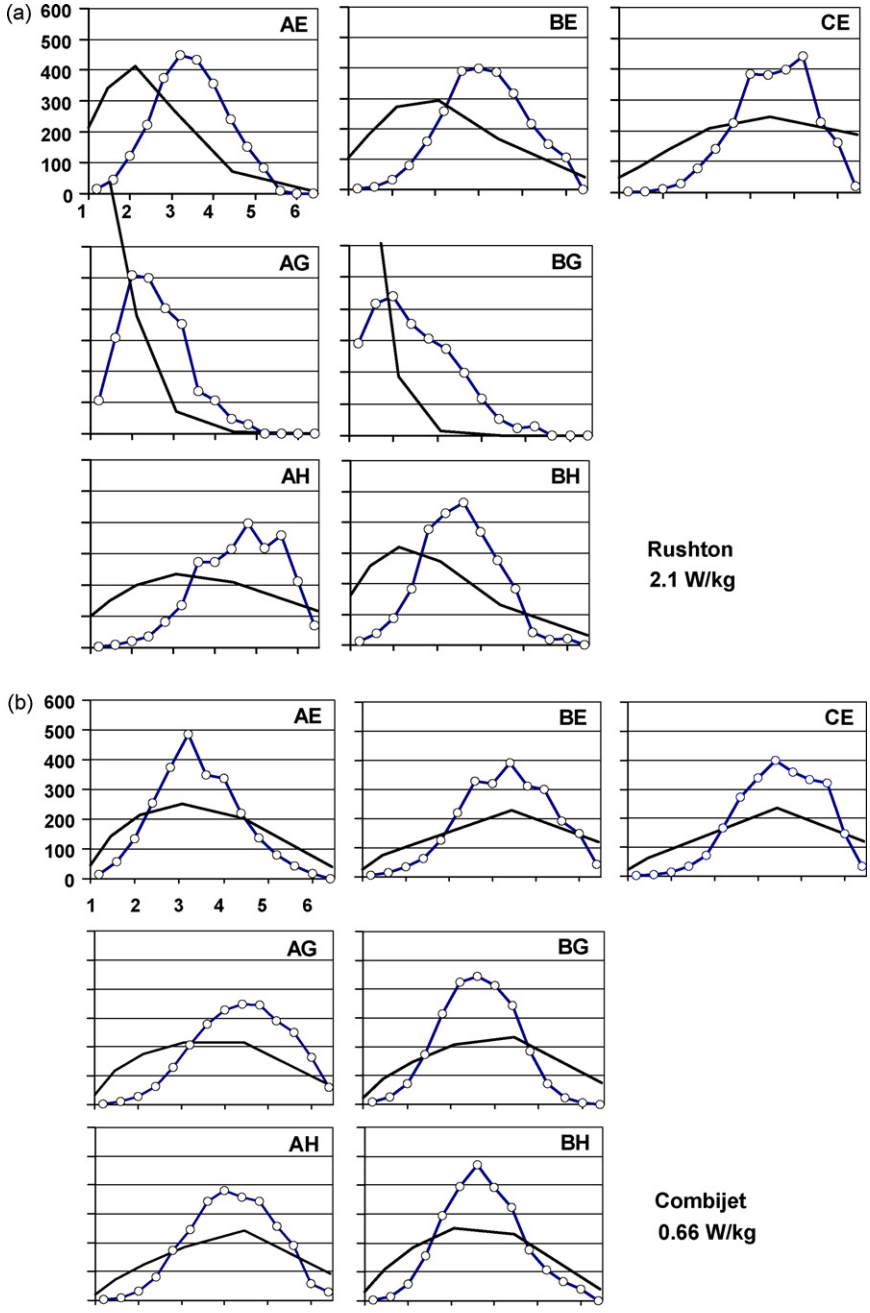

Fig. 7. Comparison between CSP experiments and CFD simulations with (a) Rushton impeller (2.1 W/kg, 0.7 vvm), (b) Combijet impeller (0.66 W/kg, 0.7 vvm), (c) Combijet impeller (2.1 W/kg, 0.7 vvm) (The impeller modelling approach is also investigated here: dashed line (sliding grid) and continuous line (MFOR).), and (d) Phasejet impeller (2.1 W/kg, 0.7 vvm). The volumetric density distribution is plotted against bubble size (mm)

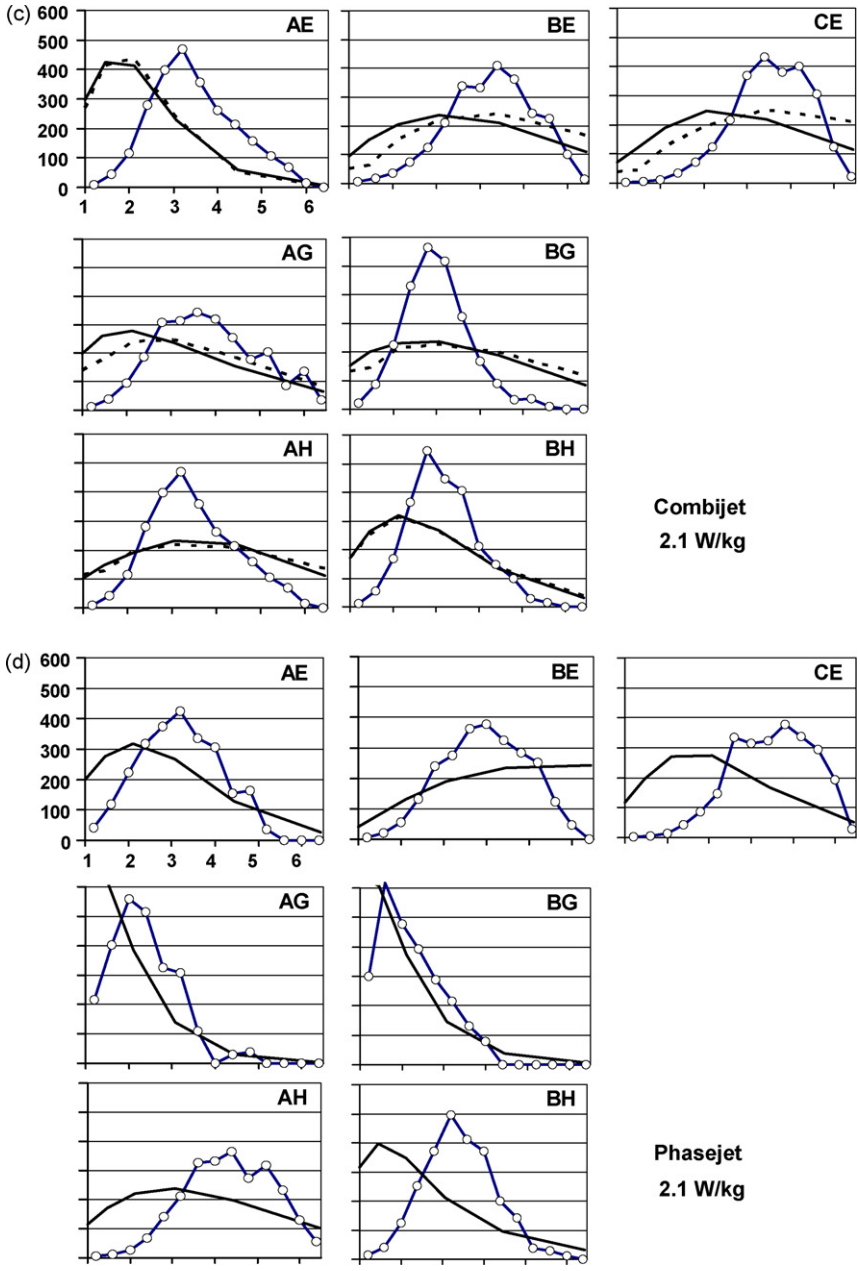

Fig. 7. (*Continued*).

so caution must be taken when drawing conclusions from the results. It has been demonstrated that the assumed gas flow pattern has a dramatic influence on the value of k_La except with the lowest gassing rates [33]. The flow-pattern is neither plug flow nor backmixed, unfortunately this means that most of the published k_La values are under suspect because of simplifications to the gas flow pattern [29]. The best way to investigate mass transfer would be to simulate saturation with nitrogen/air and monitor the dissolved oxygen, but the computational cost is too high. The simulation trends correlate well with the experimental results. The gas hold-up and mass transfer rate increase when the mixing is intensified. It seems that differences with the impeller k_La's are almost within experimental error (Table 1). With 2.1 W/kg mixing intensity (fully dispersed flow) the order is: 1, CJ; 2, PJ; 3, RT. Simulations predict the same order for the impellers, but the differences are much more pronounced. With the 0.66 W/kg mixing intensity the results were mixed, but the simulated k_La and gas hold-up are of right order of magnitude in all simulations. It is surprising that in experiments k_La of RT is at par with other impellers, even if the vessel-averaged hold-up for the CJ and PJ is larger. It is likely that the increased gas hold-up also increases bubble coalescence thus decreasing the interfacial area. Another possibility is that the large interfacial area and the turbulent energy dissipation are not located in the same places with the CJ and PJ, but without measurements this is just speculation.

The largest differences in the vessel-averaged results most likely originate from the pumping capabilities of the impellers.

Table 2
Local Sauter mean diameter (d_{32}) from experiments (normal) compared against MUSIG (parenthesis), BND (italic) and MUSIG with sliding grid (underlined)

0.66 W/kg		2.1 W/kg	
Rushton			
AE	3.47 (2.12) *1.91*	AE	3.19 (1.89) *2.58*
AG	3.04 (1.39) *1.28*	AG	2.30 (1.16) *1.47*
AH	4.35 (1.88) *2.19*	AH	4.34 (3.10) *2.96*
BE	3.89 (2.57) *2.33*	BE	3.89 (2.52) *4.08*
BG	2.62 (1.35) *1.02*	BG	2.11 (0.88) *0.92*
BH	3.37 (1.92) *1.48*	BH	3.28 (2.22) *1.63*
CE	4.14 (3.32) *3.00*	CE	4.33 (4.25) *5.67*
Averaged	3.56 (2.08) *1.89*	Averaged	3.35 (2.29) *2.76*
Phasejet			
AE	3.27 (2.21) *3.61*	AE	2.87 (2.08) *3.63*
AG	2.60 (1.77) *2.75*	AG	2.02 (1.27) *3.25*
AH	4.28 (2.84) *6.30*	AH	4.04 (2.93) *5.51*
BE	3.87 (2.94) *9.09*	BE	3.67 (6.19) *9.19*
BG	2.57 (1.90) *2.78*	BG	1.90 (1.28) *2.90*
BH	3.39 (1.71) *2.95*	BH	3.16 (1.85) *2.36*
CE	4.18 (4.93) *7.04*	CE	4.28 (2.56) *5.24*
Averaged	3.45 (2.61) *4.93*	Averaged	3.14 (2.59) *4.58*
Combijet			
AE	3.15 (2.32) *3.25*	AE	3.19 (1.75) *2.53* 1.75
AG	4.12 (3.30) *3.51*	AG	3.48 (2.39) *2.50* 2.64
AH	3.92 (3.65) *4.09*	AH	3.19 (3.03) *3.74* 3.13
BE	4.03 (5.34) *3.81*	BE	3.97 (3.25) *5.01* 4.39
BG	3.38 (3.33) *3.06*	BG	2.79 (2.59) *2.92* 2.92
BH	3.59 (2.28) *1.92*	BH	2.96 (2.23) *2.17* 2.25
CE	4.30 (5.10) *4.97*	CE	4.33 (3.46) *5.07* 4.77
Averaged	3.77 (3.62) *3.52*	Averaged	3.42 (2.67) *3.42* 3.12

The schematic of the experimental locations is presented in Fig. 6a.

A large pumping capacity means a higher liquid velocity, which means increased gas hold-up, as bubbles do not rise fast enough to escape from the flow. It can be concluded from Table 1 and Figs. 3 and 5a, that the RT generates an intensive turbulence field early in the impeller discharge flow, which generates a lot of turbulent eddies which slow the liquid flow. The vessel-averaged eddy viscosity for RT is in all cases over 60% larger (Table 1) than with the other impellers. With the CJ and PJ the turbulence is created further out in the discharge flow and spread out more evenly, resulting in more moderate eddy viscosities and faster liquid flow.

The local conditions vary spatially. To investigate the volumetric mass transfer rate, k_La, we begin from turbulent energy dissipation ε (Fig. 5a) assumed here to control the mass transfer resistance in the gas–liquid interface k_L (Fig. 5b). All the impellers generate the highest turbulence in the impeller discharge stream before the flow hits the wall. RT generates more intense turbulent dissipation in the beginning of the impeller discharge than the other impellers. The CJ generates dissipation mostly in the re-circulation below the impeller plane. The k_L for PJ and CJ is fairly well distributed around the vessel, though the highest values are in the impeller discharge. With the RT the k_L is small near the surface of dispersion and the impeller shaft, but in those areas the G–L interfacial area is also low, so this does not affect the mass transfer so much.

The G–L interfacial area a is calculated from local gas hold-up α and BSD. The gas hold-up is high in the centre of a re-circulating flow (Figs. 3 and 5c), for RT and PJ this means two toruses centred on the axis above and below the impeller plane. With CJ impeller most of the gas is accumulated in the downward flow near vessel wall below impeller plane. Above impeller plane the flow is sporadic and does not create any permanent areas of high gas hold-up. The local Sauter mean diameter d_{32} (Fig. 5d) is small in regions where turbulence dissipation is high or in regions where gas fraction is small. The mean diameter is large in regions where the gas hold-up is high due to increased coalescence or in areas where bubbles are caught in a downward flow. High mass transfer rates can be found in places where bubble size is small and turbulence energy dissipation is strong (impeller discharge) or alternatively where the gas hold-up is high and there is some turbulent energy dissipation (re-circulating flows). This heterogeneity of stirred vessels leads to very uneven mass transfer (Fig. 5e). The simulated and experimental k_La is compared against two popular correlations in Table 3. From this table it can be seen that the MUSIG results are predominantly between the k_La's calculated from experimental correlations, whereas the BND slightly underestimates the mass transfer rate. Middleton's correlation [29] gives higher k_La estimates than the Van't Riet's correlation [34] because it considers the heterogeneity of the gas phase. Based on these simulations we would expect a more

Table 3
Vessel-averaged k_La's (s^{-1}) from correlations [29,34] compared against experiments and CFD simulations, 0.7 vvm, 0.2 m^3 vessel, air–water

	Correlations			Experiments and simulations		
	Middleton	Van't Riet		Experiment	CFD (MUSIG)	CFD (BND)
0.66 W/kg	0.047	0.030	Rushton	0.039	(0.021)	*0.017*
			Phasejet	0.036	(0.029)	*0.019*
			Combijet	0.037	(0.039)	*0.029*
2.11 W/kg	0.105	0.048	Rushton	0.054	(0.054)	*0.041*
			Phasejet	0.055	(0.091)	*0.040*
			Combijet	0.058	(0.113)	*0.096*

distinct difference in the experimental k_La between the investigated impellers. The BSD comparison (Fig. 7a–d and Table 2) showed that the MUSIG simulations seem to somewhat underpredict the peak of the BSD. This smaller bubble size increases gas hold-up due to decreased bubble slip velocity, resulting in increased mass transfer rate. It must be also stated that the mass transfer areas are very sensitive to the bubble size, since the mass transfer area per air volume is inversely dependent on the Sauter mean diameter (d_{32}).

With the lower agitation rate (0.66 W/kg) a shortcoming of the MUSIG model can be clearly seen. In the areas below impeller plane the CFD simulations underestimate the mean diameter significantly. The most likely reason for this is that the small bubbles are not easily convected below the impeller plane, since the slip velocity is calculated based on the average mean diameter. We suspect that smaller bubbles are in reality convected better below the impeller plane and coalesce there to form larger ones, thus increasing the average bubble size and gas hold-up. However, this phenomenon cannot be described with the homogenous velocity MUSIG model. Recently there has been an attempt to develop a MUSIG model that does not share a common velocity field for all bubbles [35]. Further improvements may be obtained by using: more bubble classes, a large eddy turbulence model instead of RANS, case specific coalesce and breakage parameters, the simulation of the whole transient oxygen sorption/desorption simulation instead of just a pseudo steady-state and transferring components instead of simulating just the mass transfer rate. But, as this model is intended to be used for engineering and design purposes the computational demand becomes quickly too high. This model is able to provide the engineer with reasonable trends and insight to how the reactor behaves with different operating conditions and vessel geometries aiding in decision-making.

Based on these results it seems that k_La is described most accurately with a RT (Table 1). This is not surprising since most experimental data is from RT-agitated systems, and thus the model validations are mostly based on RT-agitated vessels. The experimental k_La is not significantly dependent on the vessel geometry [34,36]; however, in our MUSIG simulations the CJ and PJ impellers had categorically higher k_La's than the RT, even tough the turbulent energy dissipation was scaled according to experimental results in the PB and mass transfer model. This suggests that phenomenological models may not be as geometry independent, as so often assumed. This behaviour could be probably avoided by validating the models over a wide range of operating conditions (i.e. local hold-up and turbulent energy dissipation) and in different vessel geometries to avoid shortcomings with untraditional reactor designs.

4.5. Bubble number density simulations

The BND simulations were made in order to examine a computationally more efficient way to model gas–liquid mass transfer in stirred vessel. The results are compared against the experimental results and 10 bubble class PB simulations to investigate the mass transfer area distribution in the ves-

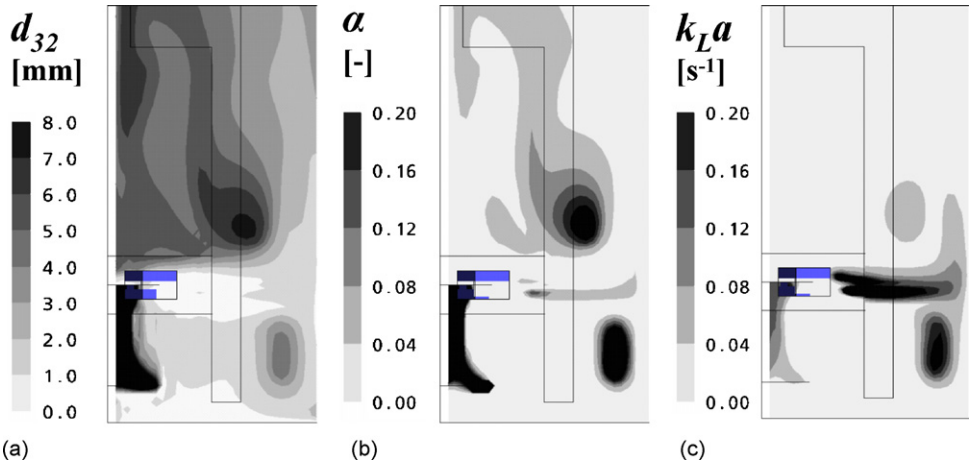

Fig. 8. (a) Local Sauter mean diameter, (b) gas hold-up and (c) volumetric mass transfer rate (RT, 2.1 W/kg, 0.7 vvm, BND).

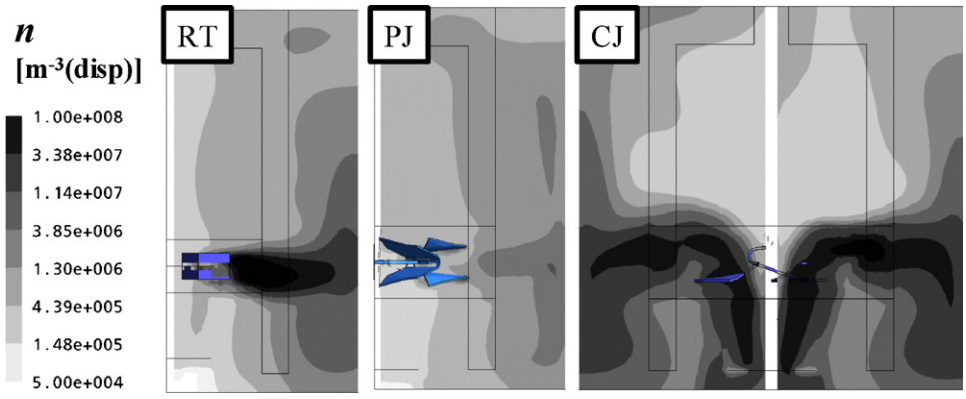

Fig. 9. Bubble number densities in the vessel with all impellers (2.1 W/kg, 0.7 vvm, BND). Note the logarithmic scale.

sel. The vessel-averaged results are presented in Table 1, local Sauter mean diameters in Table 2, and the bubble Sauter mean diameter, gas hold-up and volumetric mass transfer rate are presented in Fig. 8. The bubble number densities are presented in Fig. 9.

From the vessel-averaged results it can be seen that the bubble number density approach predicts lower k_La's than MUSIG. For RT and PJ the bubble size seems to increase with increasing agitation, which was not seen with the MUSIG approach. Otherwise the vessel-averaged results seem similar to the MUSIG simulations. The Sauter mean diameter (Fig. 8a) and gas hold-up (Fig. 8b) are very similar to Fig. 5c and d. The k_La is a bit different (Figs. 8c and 5e) since the absolute value is lower, but the shape remains same. When looking at the number densities (Fig. 9) PJ stands out, it has fewer bubbles probably due to lower turbulent dissipation at the impeller. The bubble breakage model requires a high Weber-number (>1.5) or breakage does not occur (Eq. (12)). Also the G–L interfacial area for PJ at 2.1 W/kg is only half of the corresponding value from the MUSIG simulations. All in all, the bubble number density approach produces similar results to the MUSIG model with far less computational effort, but it does not produce the local BSD like the MUSIG. It is interesting that the MUSIG and BND model predict different trends for the vessel-averaged bubble size when agitation is intensified with the RT and PJ. The bubble size decreases in the impeller discharge, but increases in areas of high gas hold-up, when agitation is intensified. Based on these experiments it is hard to say which one of the models is more accurate, since pointwise measurements do not represent the vessel-averaged value. These findings show the importance of modelling local conditions in mechanically agitated vessels. We agree with Cheung et al. [9], the BND approach is a useful and fast design tool even if it lacks the local BSD.

5. Conclusions

We assembled a set of models that allows the investigation of local variables that are difficult to measure, validate mechanistic physical models and compare different numerical solutions. It was shown that the flowfields generated by the Rushton turbine, Combijet and Phasejet are very different and the k_La is very unevenly distributed. However, the experimental k_La is not notably affected by changing the impellers. This finding is inline with the reviews of Van't Riet [34] and Yawalkar et al. [36] where it was concluded that the impeller geometry does not significantly affect k_La in a fully baffled vessel. We suspect that this levelling out of k_La is caused by increased bubble coalescence due to higher gas hold-up. The Ekato impellers provide a relatively stabile power-number with increased gassing, which makes machinery design and operation easier giving them an edge over RT.

In this work the effect of impeller geometry on G–L mass transfer (RT, CJ and PJ) was simulated with two different PB approaches (MUSIG and BND). The bubble breakage and coalescence models we used were not fitted specifically for air–water dispersions [5]. The simulations qualitatively predict the k_La with different impellers at the fully dispersed flow region. The use of sliding grid does not significantly affect the result when compared against MFOR. The BND approach provides similar results as the more complex MUSIG model with less computational effort. It was shown that the built-in CFD turbulence models were not able to describe the PJ and CJ when agitating viscous fluids, the reason remains unclear. The mass transfer rate with Rushton turbine was described more accurately than with the CJ and PJ. This behaviour could be probably avoided by validating the models over a wide range of operating conditions and different vessel geometries to avoid shortcomings in untraditional reactor designs.

Acknowledgements

Asta Nurmela, Suvi Jussila and Elina Nauha are acknowledged for the experimental measurements. Financial support from LOVI research program coordinated by the National Technology Agency of Finland (TEKES) is acknowledged. EKATO is acknowledged for providing us with the impellers.

References

[1] V.V. Ranade, Computational Flow Modeling for Chemical Reactor Engineering, Academic Press, 2002.
[2] K. Schügerl, K.H. Bellgardt, Bioreaction Engineering Modeling and Control, Springer-Verlag, Berlin, Germany, 2000.
[3] A. Bisio, R. Kabel, Scaleup of Chemical Processes, Wiley, 1985.

[4] M. Laakkonen, P. Moilanen, V. Alopaeus, J. Aittamaa, Modelling local bubble size distributions in agitated vessels, Chem. Eng. Sci. 62 (3) (2007) 721–740.
[5] P. Moilanen, M. Laakkonen, O. Visuri, J. Aittamaa, Modelling local gas–liquid mass transfer in agitated viscous shear-thinning dispersions with CFD, Ind. Eng. Chem. Res. 46 (22) (2007) 7289–7299.
[6] F. Kerdouss, A. Bannari, P. Proulx, CFD modeling of gas dispersion and bubble size in a double turbine stirred tank, Chem. Eng. Sci. 61 (10) (2006) 3313–3322.
[7] S.S. Alves, C.I. Maia, M.T. Vasconcelos, Experimental and modelling study of gas dispersion in a double turbine stirred tank, Chem. Eng. Sci. 57 (2002) 487–496.
[8] G.L. Lane, M.P. Schwarz, G.M. Evans, Numerical modelling of gas–liquid flow in stirred tanks, Chem. Eng. Sci. 60 (8–9) (2005) 2203–2214.
[9] S.C.P. Cheung, G.H. Yeoh, J.Y. Tu, On the numerical study of isothermal vertical bubbly flow using two population balance approaches, Chem. Eng. Sci. 62 (17) (2007) 4659–4674.
[10] M.L. Jackson, C.-C. Shen, Aeration and mixing in deep tank fermentation systems, AIChE J. 24 (1978) 63–71.
[11] M. Barigou, M. Greaves, Bubble size in the impeller region of a Rushton turbine, Trans. IChemE 70A (1992) 153–160.
[12] M. Barigou, M. Greaves, Bubble-size distributions in a mechanically agitated gas–liquid contactor, Chem. Eng. Sci. 47 (1992) 2009–2025.
[13] M. Laakkonen, P. Moilanen, T. Miettinen, K. Saari, M. Honkanen, P. Saarenrinne, J. Aittamaa, Local bubble size distributions in agitated vessel—comparison of three experimental techniques, Chem. Eng. Res. Des. 83 (A1) (2005) 50–58.
[14] S.S. Alves, C.I. Maia, J.M.T. Vasconcelos, A.J. Serralheiro, Bubble size in aerated stirred tanks, Chem. Eng. J. 89 (1–3) (2002) 109–117.
[15] M. Laakkonen, P. Moilanen, V. Alopaeus, J. Aittamaa, Modelling local gas–liquid mass transfer in agitated vessels, Chem. Eng. Res. Des. 85 (A5) (2007) 665–675.
[16] H. Hartmann, J.J. Derksen, C. Montavon, J. Pearson, I.S. Hamill, H.E.A. van den Akker, Assessment of large eddy and RANS stirred tank simulations by means of LDA, Chem. Eng. Sci. 59 (12) (2004) 2419–2432.
[17] B.G.M. van Wachem, A.E. Almstedt, Methods for multiphase computational fluid dynamics, Chem. Eng. J. 96 (2003) 81–98.
[18] M.V. Tabib, S.A. Roy, J.B. Joshi, CFD simulation of bubble column—an analysis of interphase forces and turbulence models, Chem. Eng. J. 139 (2008) 589–614.
[19] A. Tzounakos, D.G. Karamanev, A. Margaritis, M.A. Bergougnou, Effect of the surfactant concentration on the rise of gas bubbles in power-law non-Newtonian liquids, Ind. Eng. Chem. Res. 43 (2004) 5790–5795.
[20] T. Miyahara, S. Yamanaka, Mechanics of motion and deformation of a single bubble rising through quiescent highly viscous Newtonian and non-Newtonian media, J. Chem. Eng. Jpn. 26 (1993) 297–302.
[21] S. Lo, Application of population balance to CFD modeling of gas–liquid reactors, Trends Numer. Phys. Model. Ind. Multiphase Flows (2000) (Corse, France).
[22] H. Luo, H.F. Svendsen, Theoretical model for drop and bubble breakup in turbulent dispersions, AIChE J. 42 (1996) 1225–1233.
[23] F. Lehr, M. Millies, D. Mewes, Bubble-size distributions and flow fields in bubble columns, AIChE J. 48 (2002) 2426–2443.
[24] C.A. Coulaloglou, L.L. Tavlarides, Description of interaction processes in agitated liquid–liquid dispersions, Chem. Eng. Sci. 32 (1977) 1289–1297.
[25] K.A. Chesters, The modelling of coalescence processes in fluid–liquid dispersions: a review of current understanding, Chem. Eng. Res. Des. 69 (1991) 259–270.
[26] M. Laakkonen, P. Moilanen, V. Alopaeus, J. Aittamaa, Dynamic modeling of local reaction conditions in an agitated aerobic fermenter, AIChE J. 52 (5) (2006) 1673–1689.
[27] Q. Wu, S. Kim, M. Ishii, S.G. Beus, One-group interfacial area transport in vertical bubbly flow, Int. J. Heat Mass Transfer 41 (8–9) (1998) 1103–1112.
[28] Y. Kawase, B. Halard, M. Moo-Young, Liquid-phase mass transfer coefficients in bioreactors, Biotech. Bioeng. 39 (11) (1992) 1133–1140.
[29] J.C. Middleton, in: N. Harnby, M.F. Edwards, A.W. Niewnow (Eds.), Mixing in the Process Industries, Gas–Liquid Dispersion and Mixing, 2nd edition, Butterworth-Heinemann, Oxford, 1992.
[30] R. Sardeing, J. Aubin, C. Xuereb, Gas–liquid mass transfer a comparison of down- and up-pumping axial flow impellers with radial impellers, Chem. Eng. Res. Des. 82 (A12) (2004) 1589–1596.
[31] Y. Zhu, P.C. Bandopadhayay, J. Wu, Measurement of gas–liquid mass transfer in an agitated vessel. A comparison between different impellers, J. Chem. Eng. Jpn. 34 (5) (2001) 579–584.
[32] T. Kumaresan, J.B. Joshi, Effect of impeller design on the flow pattern and mixing in stirred tanks, Chem. Eng. J. 115 (3) (2006) 173–193.
[33] C.M. Chapman, L.G. Gibilaro, A.W. Nienow, A dynamic response technique for the estimation of gas–liquid mass transfer coefficients in a stirred vessel, Chem. Eng. Sci. 37 (6) (1982) 891–896.
[34] K. Van't Riet, Review of measuring methods and results in non-viscous gas–liquid mass transfer in stirred vessels, Ind. Eng. Chem. Proc. Des. Dev. 18 (3) (1979) 357–364.
[35] T. Frank, P.J. Zwart, E. Krepper, H.-M. Prasser, D. Lucas, Validation of CFD models for mono- and polydisperse air–water two-phase flows in pipes, in: Benchmarking of CFD Codes for Application to Nuclear Reactor Safety (CFD4NRS) Workshop, Garching (Munich), Germany, September 5–7, 2006.
[36] A.A. Yawalkar, A.B.M. Heesink, G.F. Versteeg, V.G. Pangarkar, Gas–liquid mass transfer coefficient in stirred tank reactors, Can. J. Chem. Eng. 80 (5) (2002) 840–848.